Displacement/strain measurements using an optical microscope and digital image correlation

Dongsheng Zhang
Shanghai University
Department of Mechanics
Shanghai 200444, China
E-mail: donzhang@staff.shu.edu.cn

Miao Luo
Shanghai Institute of Applied Mathematics
    and Mechanics
Shanghai 200072, China

Dwayne D. Arola
University of Maryland Baltimore County
Department of Mechanical Engineering
Baltimore, Maryland 21250

Abstract. We conduct displacement/strain measurements on the microscale using light microscopy and digital image correlation (DIC). Errors in the measurements attributed to the optical arrangement and aberration induced at high magnification are identified using a warping function. Coefficients of the warping function are determined using a simple technique that employs a precisely made orthogonal cross-grating plate. By acquiring images of the grating and identifying the nodes using subpixel techniques, a relationship between the object and the image planes is established. Thus, the displacement/strain derived by means of DIC is corrected by converting the displacement components in the image plane to the coordinate system existing on the object's surface. The approach is validated through a determination of the elastic properties of common metals; errors in estimation of the elastic modulus were within 4%. Although surface preparation generally plays a critical role in successful application of DIC, it is found to be of minimal importance under high magnification. Instead, the natural surface texture can be used with adjustment of the light incident angle. Results of the study show that DIC is a powerful tool in performing displacement/strain measurements on the microscale using a light microscope provided that an adequate correction is employed for image distortion. © *2006 Society of Photo-Optical Instrumentation Engineers.* [DOI: 10.1117/1.2182108]

1 Introduction

With the progressive reductions in the size of engineering components, there is a growing interest in measuring the structural behavior of objects on the microscopic scale. Digital image correlation (DIC) has proven to be a powerful noncontact optical method for displacement/strain measurements, and has been applied on both the meso-and macroscales (see, e.g., Refs. 1–5). Displacement/strain measurements using DIC on the microscale, however, pose new challenges.

In traditional applications of DIC on the macroscale, the object and image planes are considered to be linearly proportional. Consequently, all rays of light from a point in the object plane converge to the same point in the image plane, forming a clear image. If the object-to-image ratios in the two orthogonal directions are determined, the displacement/strain can be derived directly from the pixel locations of the corresponding points. However, if the object is close to the lens, or observations are conducted under higher magnification, there is an increasing potential for nonuniform distortion of the image.

The magnification range available from zoom lenses for common camera systems is largely tied to cost. A microscope is often the best option (and most affordable) for high-magnification (e.g., >25×) imaging systems. However, optical aberration is an important concern in imaging systems using a light microscope, especially for quantitative measurements. The camera model and camera model parameters play a key role in measurement accuracy and the extent of aberration. A pinhole camera model is typically adopted,[6] which assumes the object geometry is proportional to what is displayed on the image plane. However, due to additional radial aberrations caused by the lens, there is distortion between the image and object. Such distortions have been examined and defined as pillow distortion, barrel distortion, shear distortion, and perspective distortion.[7] When DIC is applied at the macroscale, lens aberration can be neglected because the distortion is so minor that it does not cause appreciable errors. However, in applications requiring high magnification, the aberration becomes significant and it must be removed to ensure measurement accuracy. As a result, very few applications of DIC have been reported that are based on use of a microscopic imaging system.

Schreier et al.[8] recently introduced a two-step calibration procedure to remove errors caused by lens aberration in 3-D displacement/deformation measurements using a microscope. The method incorporates a flat plate with a speckled surface that was displaced in two orthogonal directions over a series of steps to determine a warping function. Then the target was oriented differently to calibrate pinhole parameters for the imaging system using a bundle-adjustment technique. While the proposed approach enables an accurate calibration of a microscope system, it is quite complex and may be perceived as an obstacle to those wishing to adopt use of an optical microscope for micro-DIC.

This paper explores the feasibility of applying DIC for

displacement/strain measurements using a light microscope and a simple calibration procedure that incorporates a fine-pitched orthogonal cross-grating plate. A third-order polynomial warping function was constructed to describe the distortion errors in which the coefficients were determined by comparing node locations of the standard cross-grating plate with node locations in acquired images. The aberration distribution of a standard light microscope was evaluated using this approach. The calibration process is described in detail, including a validation of the approach from a series of tension experiments with common materials. In addition, important issues in applying DIC on the microscale are discussed, including surface preparation and illumination.

2 Methodology

2.1 Lens Aberration and Calibration

Lens aberration can cause distortion between the image plane and the object plane. To describe the relationship between these planes, coordinate systems are introduced for the object and image planes. The former lies on the object surface with the z axis defined by the surface normal. The latter is defined with the x and y axes in the horizontal and vertical directions of the image plane, respectively. For simplicity, the axes in these two coordinate systems are arranged parallel to each other.

For light microscopes there are a group of lenses/prisms along the optical path, rather than a single lens, and each element contributes to the error on the image plane. To simplify the problem, these elements can be considered in total as a composite virtual lens. To calibrate a pinhole camera model, numerous parameters must be determined. These are generally divided into internal and external components of an imaging system.[9] In applications of DIC, the peripheral region (around the image center) can be distorted due to lens aberration, and perspective distortion arises due to improper camera orientation or placement. Associated with those specific properties, only internal parameters such as the image magnification ratio and the lens distortion model are of interest. As the main distortions are radial and perspective related, the warping function should have first-order and second-order terms to present the distribution. Higher order terms might be used to describe the error distribution more precisely. However, Tsai[9] suggested that higher order terms might not help much and could cause instability in determining the coefficient of the warping function. As a compromise, third-order polynomial warping functions are defined to model aberration errors in the x and y directions according to

$$
\begin{cases}
\delta_x(x_i, y_i) = a_0 + a_1 x_i + a_2 y_i + a_3 x_i^2 + a_4 x_i y_i + a_5 y_i^2 \\
\qquad + a_6 x_i^3 + a_7 x_i^2 y_i + a_8 x_i y_i^2 + a_9 y_i^3, \\
\delta_y(x_i, y_i) = b_0 + b_1 x_i + b_2 y_i + b_3 x_i^2 + b_4 x_i y_i + b_5 y_i^2 \\
\qquad + b_6 x_i^3 + b_7 x_i^2 y_i + b_8 x_i y_i^2 + b_9 y_i^3,
\end{cases} \tag{1}
$$

where x_i and y_i are coordinate locations in the image plane, and a_i and b_i ($i = 0, \ldots, 9$) are coefficients to be determined. Accounting for aberration errors, the coordinates of the object and image are related by

$$x_o = R_x[x_i - \delta_x(x_i, y_i)],$$

$$y_o = R_y[y_i - \delta_y(x_i, y_i)], \tag{2}$$

where R_x and R_y are the magnification ratios in the x and y directions.

Aberration errors (δ_x and δ_y) in this paper were assessed using a precise cross-grating plate with fixed spatial frequency as a standard. Images of the grating were acquired with a microscopic imaging system at a constant magnification. The actual pixel locations of the grating nodes were then determined with subpixel precision by correlating the image with a simulated mathematical mask of the grayscale distribution at the grid points. Recent studies have shown that lens aberration occurring at the central area of the image is generally very small.[8] Thus, an undistorted image of the grid (without lens aberration) was regenerated by fitting the grating nodes near the image center. Then, the magnification ratios R_x and R_y were determined from the quotient of distances between two adjacent nodes in both object and image planes in the x and y directions, respectively. The quantities δ_x and δ_y represent the differences between the corresponding grating nodes in the virtual and actual images and are considered to be unique over the entire grating image. At each cross-grating node, two independent equations are generated according to Eq. (1). The number of the grating nodes evaluated in the image must provide a sufficient number of equations to solve for the 18 unique coefficients in the warping functions. A least-squares error approach can then be applied to derive the coefficients in the lens aberration model using the system of equations.

2.2 Digital Image Correlation with Lens Calibration

If two images are acquired before and after deformation, the displacement/strain distribution within the object's surface can be analyzed by means of image correlation. Assuming one small area on the object surface centered at (x_o, y_o) moves to a new position of (x_o', y_o'), the corresponding subset centered at (x_i, y_i) in the image plane moves to (x_i', y_i'). Even though there are differences in light intensity distribution and geometry between the image and the object due to the aberration, the gray-scale distribution around (x_i, y_i) is assumed to be unique and correlates only with the point (x_o, y_o) at the object surface. Ignoring lens aberration, the relationship between coordinates in the object and image planes are related by

$$x_o' - x_o = R_x(x_i' - x_i),$$

$$y_o' - y_o = R_y(y_i' - y_i), \tag{3}$$

where R_x and R_y are magnification constants of the image. If the gage length in each of the two orthogonal directions is defined as 2Δ in pixels, the corresponding strain components in the image can be derived from displacement components according to

$$\varepsilon_x = \frac{\partial u}{\partial x} = \frac{(x_{i+\Delta}' - x_{i-\Delta}') - (x_{i+\Delta} - x_{i-\Delta})}{2\Delta},$$

$$\varepsilon_y = \frac{\partial v}{\partial y} = \frac{(y'_{i+\Delta} - y'_{i-\Delta}) - (y_{i+\Delta} - y_{i-\Delta})}{2\Delta},$$

$$\gamma_{xy} = \frac{\partial u}{\partial y} + \frac{\partial v}{\partial x}$$

$$= \frac{(x'_{i+\Delta} - x'_{i-\Delta}) + (y'_{i+\Delta} - y'_{i-\Delta}) - (x_{i+\Delta} - x_{i-\Delta}) - (y_{i+\Delta} - y_{i-\Delta})}{2\Delta}.$$

$$(4)$$

Note that the strains can be determined using Eq. (4) in either the image or the object coordinate system, since they have a linear relationship. If the lens aberration is taken into account, the coordinate systems between image and object no longer have a linear relationship. According to Eqs. (2) and (3), the displacement on the object surface can be determined according to

$$x'_o - x_o = R_x[x'_i - x_i - \delta_x(x'_i, y'_i) + \delta_x(x_i, y_i)],$$

$$y'_o - y_o = R_y[y'_i - y_i - \delta_y(x'_i, y'_i) + \delta_y(x_i, y_i)], \quad (5)$$

where δ_x and δ_y are the aberrations obtained from lens calibration and described by Eq. (1). The realistic strain components at the object surface can be expressed using the displacement components obtained in image plane based on the preceding equations.

$$\varepsilon_x = \frac{(x'_{i+\Delta} - x'_{i-\Delta}) - (x_{i+\Delta} - x_{i-\Delta})}{(x_{i+\Delta} - x_{i-\Delta}) - [\delta_x(x_{i+\Delta}, y_i) - \delta_x(x_{i-\Delta}, y_i)]}$$
$$- \frac{[\delta_x(x'_{i+\Delta}, y'_i) - \delta_x(x'_{i-\Delta}, y'_i)] - [\delta_x(x_{i+\Delta}, y_i) - \delta_x(x_{i-\Delta}, y_i)]}{(x_{i+\Delta} - x_{i-\Delta}) - [\delta_x(x_{i+\Delta}, y_i) - \delta_x(x_{i-\Delta}, y_i)]},$$

$$\varepsilon_y = \frac{(y'_{i+\Delta} - y'_{i-\Delta}) - (y_{i+\Delta} - y_{i-\Delta})}{(y_{i+\Delta} - y_{i-\Delta}) - [\delta_y(x_i, y_{i+\Delta}) - \delta_y(x_i, y_{i-\Delta})]}$$
$$- \frac{[\delta_y(x'_i, y'_{i+\Delta}) - \delta_y(x'_i, y'_{i-\Delta})] - [\delta_y(x_i, y_{i+\Delta}) - \delta_y(x_i, y_{i-\Delta})]}{(y_{i+\Delta} - y_{i-\Delta}) - [\delta_y(x_i, y_{i+\Delta}) - \delta_y(x_i, y_{i-\Delta})]},$$

$$\gamma_{xy} = \frac{(x'_{i+\Delta} - x'_{i-\Delta}) - (x_{i+\Delta} - x_{i-\Delta})}{(y_{i+\Delta} - y_{i-\Delta}) - [\delta_y(x_i, y_{i+\Delta}) - \delta_y(x_i, y_{i-\Delta})]}$$
$$+ \frac{(y'_{i+\Delta} - y'_{i-\Delta}) - (y_{i+\Delta} - y_{i-\Delta})}{(x_{i+\Delta} - x_{i-\Delta}) - [\delta_x(x_{i+\Delta}, y_i) - \delta_x(x_{i-\Delta}, y_i)]}$$
$$- \frac{[\delta_x(x'_i, y'_{i+\Delta}) - \delta_x(x'_i, y'_{i-\Delta})] - [\delta_x(x_i, y_{i+\Delta}) - \delta_x(x_i, y_{i-\Delta})]}{(y_{i+\Delta} - y_{i-\Delta}) - [\delta_y(x_i, y_{i+\Delta}) - \delta_y(x_i, y_{i-\Delta})]}$$
$$- \frac{[\delta_y(x'_{i+\Delta}, y'_i) - \delta_y(x'_{i-\Delta}, y'_i)] - [\delta_y(x_{i+\Delta}, y_i) - \delta_y(x_{i-\Delta}, y_i)]}{(x_{i+\Delta} - x_{i-\Delta}) - [\delta_x(x_{i+\Delta}, y_i) - \delta_x(x_{i-\Delta}, y_i)]}.$$

$$(6)$$

Note that the gage length in the image plane is also a function of location due to the lens aberration. As the strain components defined by Eq. (6) are very sensitive to displacement variations, a smoothing routine was employed to suppress the noise according to Ref. 10. In this study, the displacement components were averaged over a finite area prior to estimating the strains. Then, the strain components were derived from discrete central difference derivatives of displacement.

3 Experiments

A calibration experiment was performed with a microscopic imaging system whereby the virtual strains of a plate undergoing rigid body movement were estimated. Then, the measurement precision was assessed in an evaluation of rigid body movement using DIC. A comparison of the precision was performed for white light and laser illumination. Microtensile experiments were conducted on three different materials with the microscopic imaging system to evaluate the elastic modulus and validate the approach for removing errors due to image distortion.

3.1 Materials

Tensile specimens were prepared for validation experiments from aluminum, brass, and stainless steel sheet materials. The brass and steel sheets were 0.076 mm in thickness and the aluminum sheet had a thickness of 0.13 mm; each sheets had brushed surface finish. Four aluminum and three brass and stainless specimens were prepared. Straight-sided tensile specimens were prepared with gage lengths ranging from 4 to 8 mm with average width of approximately 1 mm. No artificial speckle patterns were deposited or prepared on the surfaces prior to the tensile tests. An orthogonal cross-grating glass plate with spatial frequency of 10 line/mm was used in the calibration experiments. Each dark line of the grating has a width of 0.02 mm.

3.2 Equipment and Procedures

A microscopic imaging system was used for the experiments and was comprised of a Nikon SMZ800 light microscope, a monochrome 8.5-mm CCD camera, and a PCVISION plus image grabber. The light microscope has a single output for a video camera. With a fixed zoom ratio of 6.3:1, a 1× objective lens, and a 1× step-up ring at the output, one can achieve up to 180× magnification using the aforementioned camera. Digital images were obtained throughout the experiments with 8-bit intensity and resolution of 640×480 pixels. The system can be used for a field of view as small as 0.8×0.6 mm, resulting in a spatial resolution of approximately 1.3 μm/pixel. Two light sources were used separately in the experiments, i.e., white light fiber optics and a He-Ne laser.

Calibration of the imaging system was conducted using the orthogonal cross-grating plate. The plate was placed horizontally under the light microscope and the camera was oriented such that the x and y axes of the image plane coincide with the corresponding axes of the object plane (Fig. 1). A simple alignment was performed by rotating the grating plate so that the grating lines were parallel (and perpendicular) to the image axes. The magnification was set to obtain a field of view of 2×1.5 mm, resulting in a spatial resolution of 3.1 μm/pixel. An example of the sampled grating image at this magnification is shown in Fig. 2.

Following the calibration experiments, an aluminum sheet was bonded on a 2-D translation stage with the same relative magnification. The stage was aligned such that the axes of translation coincided with the axes of the image plane. Illumination of the plate was achieved using either
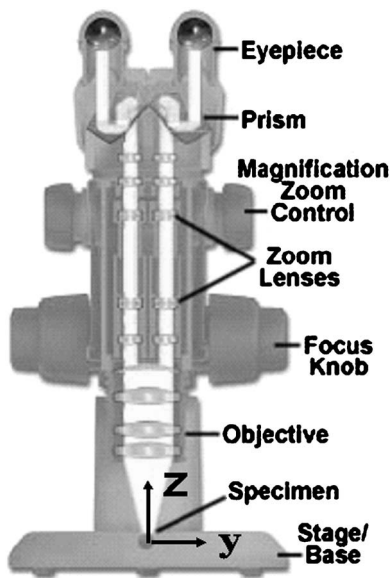
Fig. 1 Schematic diagram for the light microscope (Courtesy of Nikon).

an unexpanded He–Ne laser beam or a fiber optical illuminator. Translation of the plate was performed in increments of 0.025 mm along either the x or y directions and digital images were documented after every step of translation. The displacement field was evaluated using DIC and the virtual strains were computed according to Eq. (6). Errors in the measured displacements were then quantified with regard to the two methods of illumination.

A motorized miniature load frame was developed for the microtensile experiment, which can work in both load control and displacement control modes with a fine-tunable rate. The system has a load range of up to 100 N with load precision of 0.05%. The master computer controls both the load frame and imaging system to enable real-time data acquisition while also simultaneously sampling sequential images. The experimental setup for the microtensile experi-
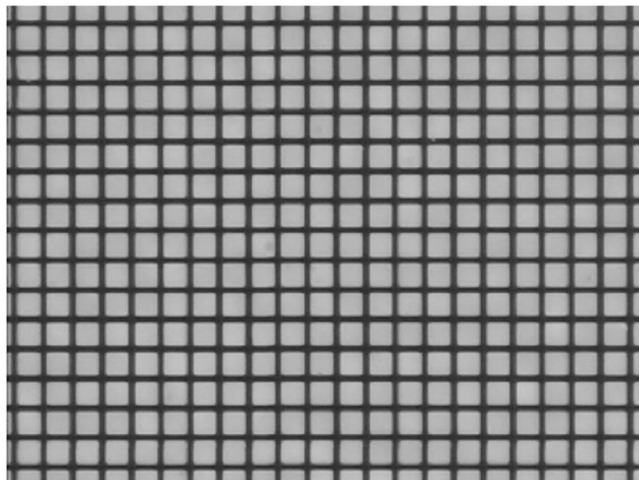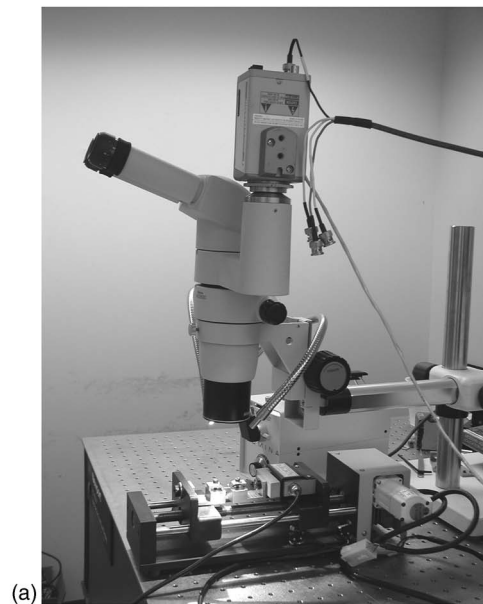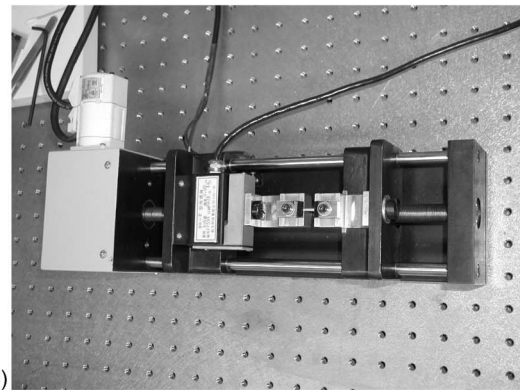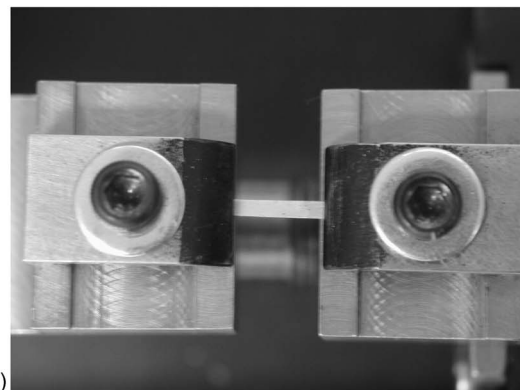

Fig. 3 Experimental system used for the microtensile tests: (a) the optical test system and microtensile frame, (b) the microtensile frame, and (c) a tensile specimen mounted with the compressive grips.

ment is shown in Fig. 3(a). The miniature load frame [Fig. 3(b)] was oriented such that the direction of elongation agrees with the x axis of the image plane. Compressive grips were used to clamp the tensile specimens, as shown in Fig. 3(c), and the specimens were loaded in displacement control mode at a rate of 0.4 mm/min. Sequential digital images were acquired from the onset of loading of 0.25 Hz and the load was sampled at 20 Hz. All sequential images
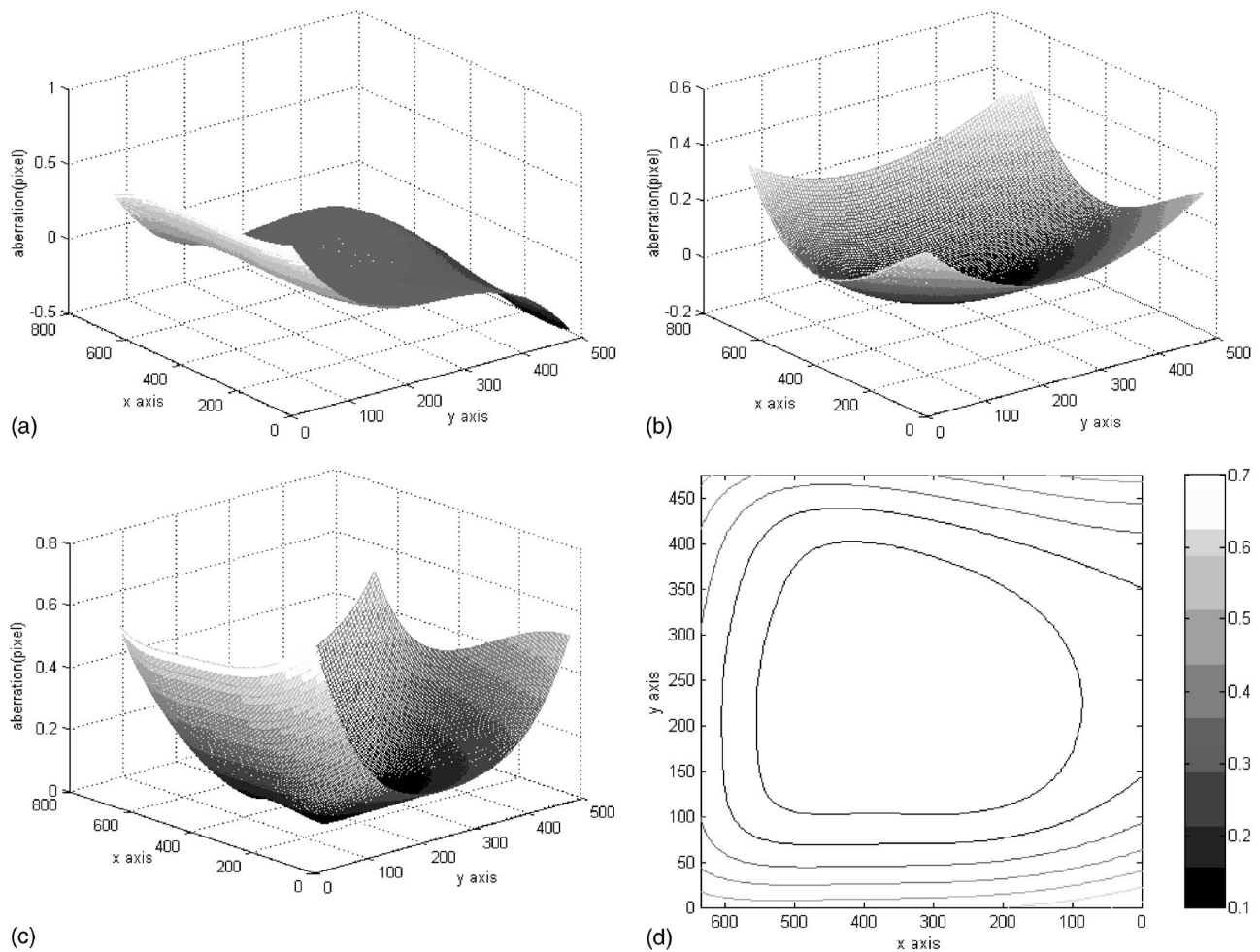

Fig. 2 Image of the grating taken by the microscopic imaging system. The center to center grid distance is 0.1 mm.

Fig. 4 Lens aberration distribution of the light microscope: (a) aberration in the *x* direction, (b) aberration in the *y* direction, (c) total magnitude of aberration, and (d) aberration contour map. Units for both the *x* and *y* axes are pixels.

were taken at a constant magnification and an image of the cross-grating was taken after the tensile test to determined the magnification ratio. In addition, the surface topography of the tensile specimens was evaluated using a Zygo 3-D profilometer. The average surface roughness (Ra), peak to valley height surface roughness (Ry) and root mean square roughness (Rq) were assessed at five random spots and then averaged for each material examined.

4 Results

The warping error distribution (δ_x, δ_y) over the entire image is shown in Fig. 4. In particular, the warping error distribution in the *x* and *y* directions is shown in Figs. 4(a) and 4(b), respectively. The resultant error and a contour plot of the resultant error distribution are shown in Fig. 4(c) and 4(d), respectively. As expected, the error at the central area of the image is far less than that at the four corners. Although light microscopes are comprised of multiple optical elements, the aberration distribution is similar to that of a single lens. Interestingly, however, the error distribution in the two directions (*x*, and *y*) is quite different, based on the unique features of the microscope. The physical design of the stereo light microscope (Fig. 1) incorporates two inde-

pendent light paths. When one video output is mounted to enable image acquisition from either of these two beams, there is an inclination angle between the light path and the surface normal of the specimen, which lies in the horizontal plane beneath the microscope. Consequently, the error distribution is not perfectly axisymmetric due to the misalignment.

In the experiments involving rigid body movement, images were obtained with either He–Ne laser or white light illumination. The images were processed using DIC and results of the analysis are listed in Table 1.

The sequential images of each tensile specimen were analyzed with an automatic DIC algorithm.[11] The strain distribution was calculated according to Eq. (6) and the tensile stress was estimated from the load and the initial cross-sectional area of the specimens. The moduli of elasticity for the three materials were obtained from the experimental results and are listed in Table 2. The average elastic modulus for each metal estimated from the experimental results is in very good agreement with the values reported in standard handbooks.[12]

Table 1 The comparison of illumination with the rigid body movement.

	Laser Illumination (pixels)				White Light Illumination (pixels)			
	X dis	X std	Y dis	Y std	X dis	X std	Y dis	Y std
1	0.00	0.00	0.00	0.00	0.00	0.00	0.00	0.00
2	6.45	0.09	5.95	0.14	6.25	0.09	5.83	0.13
3	12.48	0.17	12.00	0.27	12.38	0.17	11.94	0.27
4	19.18	0.26	18.37	0.42	18.90	0.25	18.32	0.41
5	25.53	0.34	24.89	0.56	25.48	0.34	24.86	0.56
6	32.25	0.43	31.06	0.70	32.14	0.42	30.91	0.70
7	38.31	0.50	37.33	0.84	38.29	0.50	37.33	0.84
8	44.63	0.59	43.62	0.98	44.59	0.59	43.61	0.98
9	50.68	0.67	49.89	1.13	50.54	0.67	49.83	1.12

5 Discussion

Experimental activities focused on calibration of the optical system and development of coefficients for the warping functions showed that the stereo microscope was subject to lens aberration and resulted in distortion errors. Thus, for loading conditions that invoke rigid body movement only, aberration errors could be interpreted as "virtual displacements" or "virtual strains" in the structure. Virtual strains were determined from the derivatives of aberration errors (δ_x, δ_y) that were estimated according to Eq. (1); the strains in the x and y direction are shown in Figs. 5(a) and 5(b), respectively. The resultant virtual strain and a contour map of the distribution are shown in Figs. 5(c) and 5(d), respectively. Similar to the aberration error distribution, the virtual strains at the center part of the image are minimal, while virtual strains at the periphery are much greater. In fact, the stereo microscope used in this study resulted in errors in the y direction as large as 2000 microstrains in the corners of the image. The errors are due to the combined

Table 2 The tested Young's moduli of three metal sheets.

Measurement	Aluminum (GPa)	Brass (GPa)	Stainless Steel (GPa)
1	70.2	105.1	218.2
2	72.8	109.8	216.6
3	72.3	103.3	210.5
4	74.5		
Average	72.5	106.1	215.1
Error	1.8	3.5	7.5
Value from handbook	72	110	200

contribution of lens aberration and inclination of the optical path. As is evident in Fig. 5(d), there is a larger central area in the x direction with small virtual strains. The majority of error has resulted from optical path inclination with respect to the y axis. It is possible (and appropriate) to maximize the area with minimal aberration errors for in-plane displacement/strain measurement by simply adjusting the testing direction of the specimen. If a calibration is not performed the minimal error can be obtained from the central portion of the image.

Illumination is another concern in application of DIC for microscale measurements. The significance of illumination and light source was examined by comparing the displacement of an aluminum specimen illuminated using an unexpanded laser beam or white light from a fiber optic illuminator. Experimental results (Table 1) indicated that there were no appreciable differences with the illumination sources when the specimen surface is under planer rigid body movement up to 50 pixels of displacement. That corresponds to approximately 203 μm of displacement, since the increment of the translation is 25.4 μm. The surface contrast resulting from illumination with the laser beam was much higher than that by fiber optic illumination due to interference of the coherent light. However, the correlation coefficient derived from the laser illumination was not as high as that obtained when using white light and is likely attributed to instability in the laser intensity, either emitted from the He–Ne laser or transmitting along the optical path. Consistent with the distortion analysis, errors in the y direction were larger than those in the x direction due to the inclination angle of the binocular microscopic system. To minimize errors due to inclination, the specimen or microscope can be tilted so that the normal of the surface is aligned with the optical path of the video camera.

The Young's moduli for the aluminum, brass, and stainless steel that resulted from experiments using micro-DIC were 72.5, 106.1, and 215.1 GPa, respectively (Table 2). The elastic modulus reported in handbooks (e.g., Ref. 12)
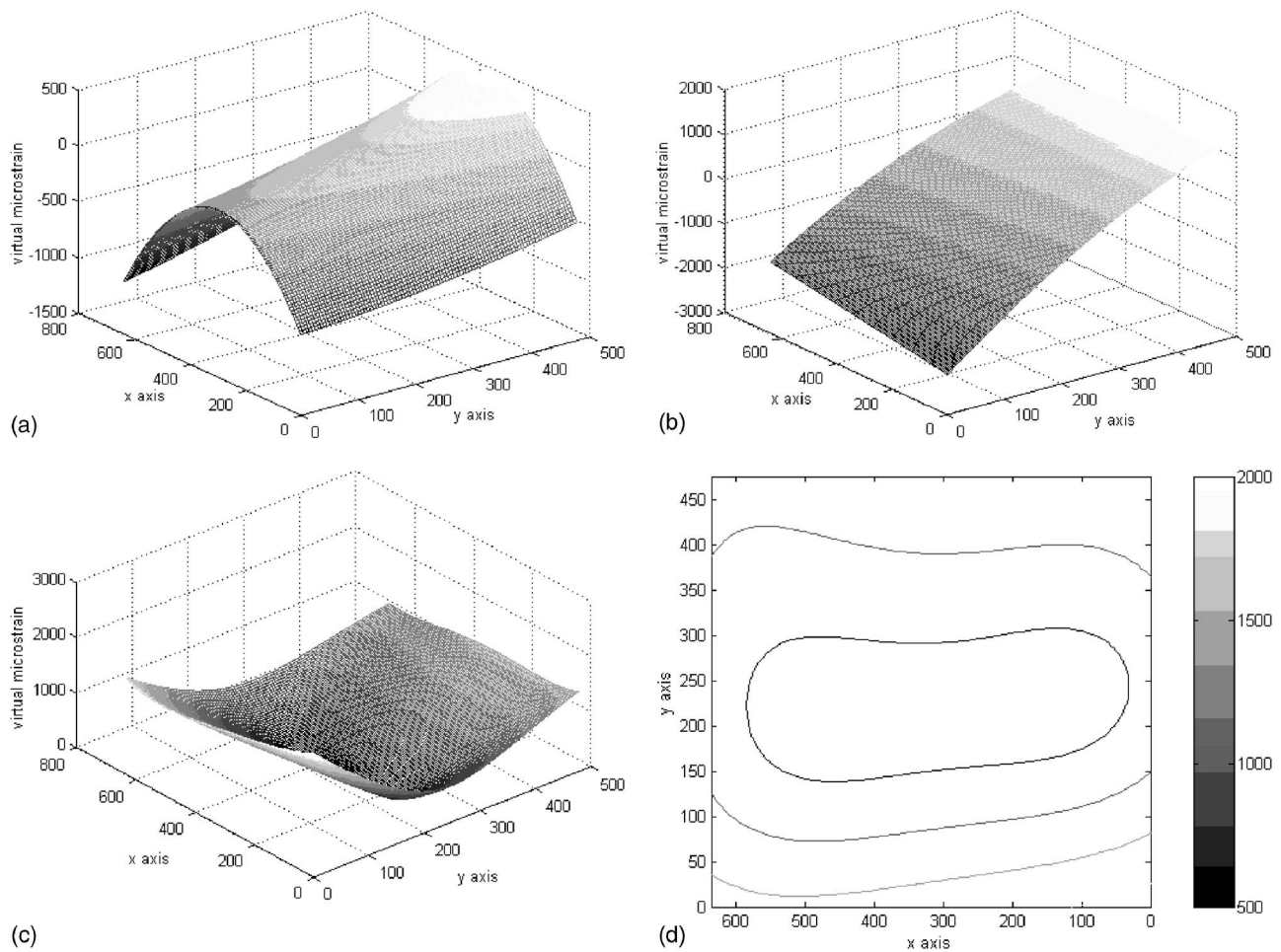
Fig. 5 Virtual strain distribution caused by lens aberration: (a) virtual strain in the *x* direction, (b) virtual strain in the *y* direction, (c) total magnitude of virtual strain, and (d) virtual strain contour map. Units for both the *x* and *y* axes are pixels.

for the aluminum, brass, and stainless steel are 72, 110, and 200 GPa, respectively. According to Dowling,[13] the coefficient of variation (COV) in experimental estimates for an elastic modulus, which is estimated from the ratio of the standard deviation and average value, is near 0.05. The COV for the aluminum and brass (Table 2) are both less than 0.05 and provide added confidence in the experimental approach; for stainless steel, the COV is greater than 0.075. Note that the specimen cross sections were measured using dial calipers and that slight measurement errors could contribute to systematic errors in estimations of Young's modulus. It is important to use a precise measurement technique when conducting experiments on the mesoscale.

Surface preparation is generally regarded as an integral part of displacement/strain measurements using DIC. The speckled surface is the information carrier and a necessary component for image correlation. Traditional methods of surface preparation, which include application of fine powder[8] or spraying paint[11] onto the specimen surface, have proven to be effective. However, they are no longer applicable for microscale measurements; speckles resulting from spray paint or powder particles are exaggerated at high magnification and can cause focusing problems. The size of the speckles is of another concern in correlation. In

addition, surfaces that are processed with fine sandpaper or that have been purposely scratched are not appropriate for
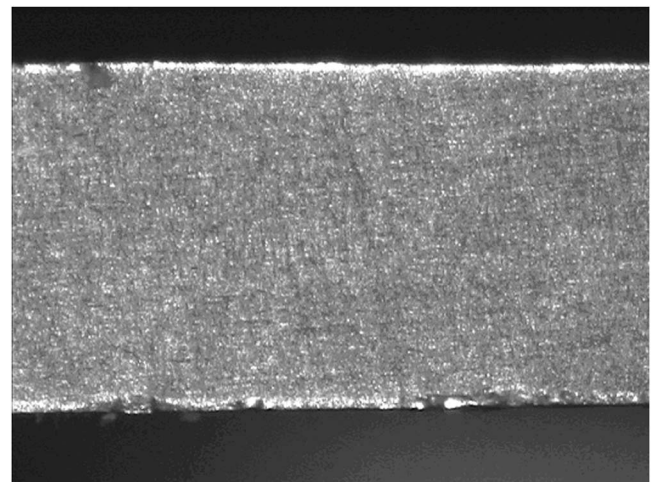

Fig. 6 Speckle image of a tensile specimen without surface preparation under the light microscope.

Table 3 The surface roughness profilometry measured by Zygo.

Measurement	Aluminum sheet			Stainless Steel Sheet		
	Ra (μm)	Ry (μm)	Rq (μm)	Ra (μm)	Ry (μm)	Rq (μm)
1	0.431	39.905	1.179	0.180	3.516	0.231
2	0.447	8.694	1.178	0.140	2.821	0.176
3	0.376	10.329	1.113	0.124	2.946	0.159
4	0.409	7.727	1.026	0.133	3.049	0.166
5	0.915	8.630	1.662	0.124	2.844	0.157

Ra: the average surface roughness; Ry: the peak to valley height roughness; Rq: the root mean square surface roughness.

DIC due to an over saturation of reflected light from the scratched edges. An example speckle image from an aluminum sheet without surface preparation is presented in Fig. 6. Fortunately, through adjustment of the angle of illumination the natural texture of the object surface appears granulated under illumination with a light microscope. The surface topography of the aluminum sheet is shown in Fig. 7 over an area of approximately 0.167×0.125 mm. Surface roughness parameters for the aluminum and stainless steel sheets used in the experiments are listed in Table 3. Although the sheet metals appeared quite smooth under the naked eye and to the touch, the microscopic surface irregularities provide an adequate texture for generation of a high-contrast speckle image. Thus, surfaces with small topographical variations are good enough to achieve high correlation.

6 Summary

This paper explored the feasibility of applying DIC for displacement/strain measurements on the microscale using a light microscope. A simple calibration procedure was introduced for removing image distortion attributed to the lenses and prisms of a light microscope. The process consisted of performing a calibration using a precision-machined cross-grating plate and development of warping functions that describe the error distribution. Similar to aberration errors resulting from a single lens, the largest aberration errors were located at the periphery of the digital images. Aberration errors resulted in distortion of the digi-

tal images and, in application of DIC, result in the appearance of "virtual displacements" or "virtual strains" in the structure. By performing a calibration using a precision cross-grating and development of warping functions to describe the distortion distribution, DIC can be applied for in-plane displacement/strain measurements. Although surface preparation is generally required for measurements of displacement or strain using DIC, the natural surface topography is sufficient for microscopic measurements using proper illumination of the surface. White light illumination should be used with an adjustment of the angle of incidence to generate a surface with a large range in gray-scale intensity. An unexpanded laser beam can also be applied to illuminate to produce a speckled surface with high contrast if stable laser illumination can be achieved.

Fig. 7 Surface topography of an aluminum tensile specimen.

References

1. M. A. Sutton, Y. J. Chao, and J. S. Lyons, "Computer vision methods for surface deformation measurements in fracture mechanics, novel experimental techniques in fracture mechanics," *AMD (Am. Soc. Mech. Eng.)* **176**, 123–133 (1993).
2. H. Lu, G. Vendroux, and W. G. Knauss, "Surface deformation measurements of a cylindrical specimen by digital image correlation," *Exp. Mech.* **37**(4), 433–439 (1997).
3. W. Zhao and G. Jin, "An experimental study on measurement of Poisson's ratio with digital correlation method," *J. Appl. Polym. Sci.* **60**(8), 1083–1088 (1996).
4. D. Zhang, X. Zhang, and G. Cheng, "Compression strain measurement by digital speckle correlation," *Exp. Mech.* **39**(1), 62–65 (1999).
5. M. A. Sutton, S. R. McNeil, J. D. Helm, and H. W. Schreier, "Computer vision applied to shape and deformation measurement," in *Proc. Int. Conf. on Trends in Optical Non-Destructive Testing and Inspection*, pp. 571–589, Lugano, Switzerland (2000).
6. O. Faugeras, *Three-Dimensional Computer Vision: A Geometric Viewpoint*, MIT Press, Cambridge, MA (1993).
7. Q. Yu, D. Zhang, Z. Lei, and T. Quan, "Accurate measurement of 3D coordinate of an object with subpixel technique," in *Proc. IEEE Int. Conf. on Systems, Man and Cybernetics*, Vol. **1**, pp. 484–486 (1996).
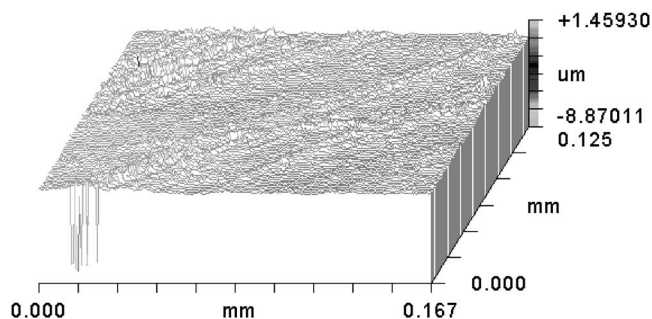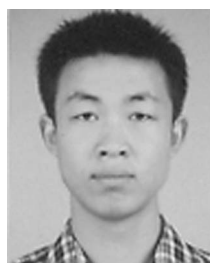8. H. W. Schreier, D. Garcia, and M. A. Sutton, "Advances in light

microscope stereo vision," *Exp. Mech.* **44**(3), 278–288 (2004).
9. R. Y. Tsai, "A versatile camera calibration technique for high-accuracy 3D machine vision metrology using off-the-shelf TV camera and lenses," *IEEE J. Rob. Autom.* **RA-3**(4), 8323–8344 (1987).
10. W. Tong, "Detection of plastic deformation patterns in binary aluminum alloy," *Exp. Mech.* **37**(4), 452–459 (1997).
11. D. Zhang, D. Arola, P. G. Charalambides, and M. C. L. Patterson, "On the mechanical behavior of carbon-carbon optic grids determined using a bi-axial optical extensometer," *J. Mater. Sci.* **39**, 4495–4505 (2004).
12. F. Cardarelli, *Materials Handbook. A Concise Desktop Reference*, Springer Verlag, London (1999).
13. N. E. Dowling, *Mechanical Behavior of Materials*, 2nd ed., Prentice Hall, (1998).

Miao Luo is a graduate student with the Department of Mechanics, Shanghai University, China. His research is focused on the application of digital image correlation at the micro scale.

Dongsheng Zhang is a professor with the Department of Mechanics, Shanghai University, China. He received his BS and MS degrees from National University of Defense Technology, Changsha, China, in 1987 and 1990, respectively, and his PhD degree from Tianjin University in 1993. His research interests include precision optical measurement, biomechanics, and experimental mechanics.

Dwayne D. Arola is an associate professor with the Department of Mechanical Engineering, University of Maryland Baltimore County. He received his BS, MS, and PhD degrees from University of Washington in 1989, 1991, and 1996, respectively. His research interests include fatigue and fracture, biomechanics, and experimental mechanics.